International Journal of Heat and Mass Transfer 161 (2020) 120310

Contents lists available at ScienceDirect

International Journal of Heat and Mass Transfer

journal homepage: www.elsevier.com/locate/hmt

Visualizing the vibration effect on the tandem-pulsed gas metal arc welding in the presence of surface tension active elements

H. Hamed Zargari[a,*], K. Ito[a], M. Kumar[b], A. Sharma[c]

[a] Joining and Welding Research Institute (JWRI), Osaka University, Ibaraki 567-0047, Japan
[b] Indian Institute of Technology Hyderabad (IITH), Sangarddey, Hyderabad 505 285, India
[c] KU Leuven, Faculty of Engineering Technology, Department of Materials Engineering, Campus De Nayer, 2860 Sint-Katelijne-Waver, Belgium

ARTICLE INFO

Article history:
Received 23 May 2020
Revised 16 July 2020
Accepted 9 August 2020
Available online 20 August 2020

Keywords:
Pulsed gas metal arc welding
Vibration
Tandem welding
Numerical simulation
Surface tension

ABSTRACT

In this study, a three-dimensional model of the tandem-pulsed gas metal arc welding process is simulated to investigate the heat transfer and material flow in the presence of vibration and the surface tension active elements. The simulation results are in agreement with optical microscopy images of weld cross-section obtained with different conditions, including with and without vibration-assisted welding. The material flow is visualized using 2D and 3D streamlines on the temperature contour maps. It is found that during the operation of pulsed welding, the heat follows a very stable pattern, although the fluid streams continuously change in the rear region of the weld pool, which is responsible for the final geometry of penetration. Consideration of the effect of surface tension active elements on the Marangoni force improves the simulation results noticeably. A novel approach addresses the effect of sulfur content that comes from both workpiece and filler material. Applying the vibration leads to lower heat input by affecting the free surface behavior and plays an important role in the penetration shape change.

1. Introduction

The tandem gas metal arc welding (GMAW) is one of the welding techniques with application in heavy and automotive industries due to higher productivity and deposition rate in comparison to conventional single wire cases. Employing the pulsed arc feature allows the use of smooth and spatter free conditions of welding in addition to special productivity function [1]. Despite all the advantages, the penetration shape of the weld metal and the microstructure of heat affected zone (HAZ) are not always as desirable, for example, the finger-type penetration occurs even in the mid-range current, which affects the mechanical properties of weld metal. Many studies on the characterization of the welds controlled by different current waveforms [2–4] and vibration-assisted welding (VAW) [5] have been conducted.

The molten pool oscillation in the case of GMAW has been investigated from various points of view over the past years [2,6]. The analytical models supported by experimental observation led to the development of an oscillation based control system [7]. On the other hand, the workpiece vibration as a kind of VAW controls the microstructure of the weld metal and HAZ, such as morphological modification, and reducing residual stresses, and leads to improved mechanical properties in the weld zone [5,8]. Incidentally, it was found that the finger-type fusion zone transformed into a pan bottom shape when applying longitudinal sine-mode of workpiece vibration to the single wire pulsed GMAW [9,10]. Further investigation on the tandem wire pulsed GMAW revealed the effect of various frequencies and the existence of a specific frequency (around 250 Hz) to create the optimal pan bottom shape. The complicated conditions of tandem-pulsed gas metal arc welding (TP-GMAW) need a different method for visualizing the heat and mass transfer through the weld pool. Due to the complex conditions of GMAW, there is a high potential for using the numerical model to isolate and investigate the importance of each parameter during the process. However, with similar arguments, the interaction between the forces can simply conceal the various types of faults in the model and can lead to a pseudo-balance in the weld pool. Therefore, a high degree of accuracy in the determination of various input parameters such as heat distribution, welding efficiency, the physics of droplet, and the surface tension coefficient is needed before analyzing the numerical results.

To reveal the inside characters of the fusion zone, the Finite Difference Method (FDM) is used by the investigators with governing equations of mass, momentum, and energy conservation [11,12]. Further, the volume of fluid technique (VOF) is employed for tracking the free surface of the molten pool; first introduced by Hirt and Nichols based on the donor–acceptor approach [13]. Cao and

* Corresponding author.
E-mail address: habibi@jwri.osaka-u.ac.jp (H. Hamed Zargari).

https://doi.org/10.1016/j.ijheatmasstransfer.2020.120310
0017-9310/

Yang [14] developed a three-dimensional model of GMAW using the VOF technique. Cho et al. [15] expanded the VOF-based model for pulsed GMAW by the precise definition of input variables. Hu et al. [16], in a comprehensive study, simulated the ripple formation in GMAW. Most of the numerical simulations in this period suffered from the accuracy of the standard VOF algorithm in the identical weld pool conditions. In more detail, the behavior of free surface in the longitudinal cross-section was still far from the images taken by the high-speed camera, especially once the droplet impinged the surface of the weld pool. Different kinds of enhancements have been made to the initial algorithm of VOF due to the possibility of overfilling or over-emptying computational cells in the special conditions [17–19]. Among all the enhancement algorithms, the Lagrangian based VOF advection exhibits good accuracy in tracking sharp interfaces in complex three-dimensional motions with the surface tension [20]. Utilizing the potential of new algorithms, the analysis of fusion welding was performed in good agreement with the experimental results [21]. However, the improvement in the GMAW models is still under demand for the application such as hybrid welding and the examination of special methods [22,23].

Despite various numerical models investigating the single wire GMAW [21,24], the mechanism of deep finger-type fusion zone in tandem-wire welding is not clearly understood based on the numerical scheme. It was found that ignoring the well-known phenomena, i.e. change in the gradient of surface tension coefficient [25–28], plays an important role in the inaccurate penetration by the new research based on the VOF method. Albeit, the effect of surface-active elements during metal-based additive manufacturing has been taken into consideration in the latest articles [29,30]. The current study demonstrates how the input variables, such as surface tension coefficients associated with the mathematical algorithm, can affect extremely the predicted final geometry of the weld pool. Furthermore, the effect of specific vibration condition on the penetration shape in TP-GMAW is discussed. The numerical model simulated with and without vibration of the workpiece is supported by the experimental results. To generate the mesh-independent model with the highest accuracy of surface tension effect, the fine cubic mesh with a cell size of 0.15 mm was employed. A novel three-dimensional simulation considering the workpiece vibration and TP-GMAW interactive phenomena is successfully performed for the first time.

2. Experimental procedure

The welding experiments were conducted using a robotic TP-GMAW facility at IIT Hyderabad in which two electrodes are separately fed through the welding torch and received the power from two independent power sources. The power sources were synchronized in an anti-phase manner to prevent mutual interaction between the trailing and leading arcs. Ar 82% – CO_2 18% was used as a shielding gas. The robotic welding facility consisted of a 6-axis robot of KR30 of KUKA make, which was connected with two digital welding power sources of Fronius make. The currents at the trail and lead electrodes were set equal to 180 A. The bead-on-plate welding for a length of 200 mm was performed in a flat position by keeping the welding torch normal to the workpiece. The base material used in the present work was a hot rolled low carbon steel IS 2062-2011 consisting of the ferrite-pearlite structure. The wire electrode was ER 70-S of 1.2 mm in diameter. The chemical compositions of the base metal and welding wire are listed in Table 1. The Sdyn Electro-dynamic Vibration machine of 1500 kgf capacity was used for the vibration generation.

The slip table connected to the shaker head was vibrated at 250 Hz in the welding direction. Four wedge clamps were used evenly to fix the workpiece tightly to avoid any kind of distortion during welding. The continuous sine-mode vibration was applied in the longitudinal direction to the weld seam. The welding equipment is shown in Fig. 1. More details of torches circumstances and the vibration condition will be discussed in Section 3.3. The cross-sectional macroscopic examination of as-welded specimens was conducted using optical microscopy (OM) after polishing and etching by 7 vol% HNO_3 + 93 vol% CH_3OH. The welding parameters, including the pulse and the vibration characteristics, are listed in Table 2. The current–voltage waveforms of leading and trailing electrodes, recorded at a frequency of 5 kHz, are shown in Fig. 2. The waveforms show stable signals observed over the entire weld length, except for the start and end of the weld.

Table 1
The composition of base materials and filler wires (wt%).

	C	Si	Mn	P	S	Fe
IS2062-2011	0.211	0.206	0.71	0.015	0.018	Bal.
ER70S-6	0.07-0.15	0.80–1.15	<1.85	<0.025	<0.035	Bal.

Table 2
TP-GMAW and vibration parameters.

Parameter	*Value*	*Parameter*	*Value*
Current set (Lead, Trail)	180, 180 A	Contact-tip-to workpiece-distance	20 mm
Current type	Pulsed DCEP	Travel speed	1.2 m/min
Pulse frequency	154 Hz	Electrodes distance	8 mm
Pulse time (Duty)	3.2 ms	Gas rate per cylinder	12 L/min
Tandem interval	2.2 ms	Vibration acceleration	1.2 m/s^2
Wire diameter	1.2 mm	Vibration frequency	250 Hz
Wire feed average	2×7.4 m/min	Vibration amplitude	0.5 μm

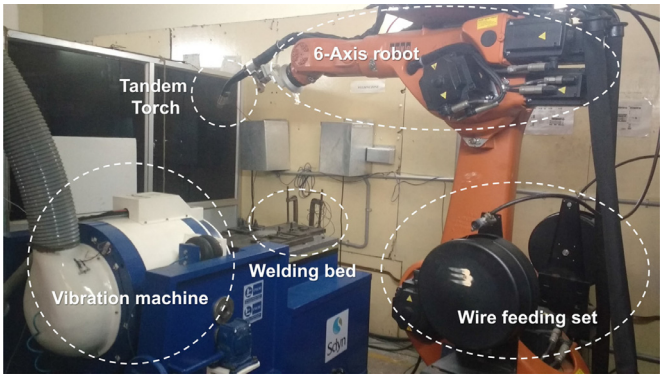

Fig. 1. The welding equipment and supplementary vibration machine.

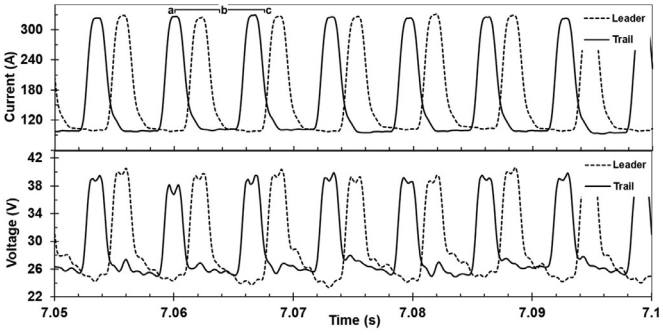

Fig. 2. The current–voltage waveform of leading and trailing electrodes in W/O vibration.

3. Mathematical modeling and formulation

3.1. Governing equations

A three-dimensional Cartesian model is developed to analyze the profile and convection in the weld pool obtained with the TP-GMAW process. A laminar flow of Newtonian and incompressible fluid is considered in the computational domain supporting the phase change capability. The molten pool is driven by a combination of electromagnetic, buoyancy, and surface tension forces. To simplify the numerical model, the effect of plasma heat on the droplets is considered by the initial temperature of the droplet. With these assumptions, a total of four governing equations including the continuity of mass, momentum (Navier–Stokes), energy conservation, and the VOF are solved together according to Eqs. (1) to (4), respectively [22]. A list of variables is described in Table 3. To analyze the heat transfer and the weld pool profile, the FLOW-3D commercial software is employed especially because of high accuracy to track the moving free-surface by the Lagrangian VOF advection method [20].

$$\frac{\partial \rho}{\partial t} + \nabla.\left(\rho \vec{V}\right) = \dot{m}_s \rightarrow \nabla.\vec{V} = \frac{\dot{m}_s}{\rho} \tag{1}$$

$$\frac{\partial \vec{V}}{\partial t} + \vec{V}\cdot\nabla\vec{V} = -\frac{1}{\rho}\nabla P + \frac{\mu}{\rho}\nabla^2\vec{V} - k_d\vec{V} + G_b + \frac{\dot{m}_s}{\rho}\cdot\left(\vec{V}_s - \vec{V}\right) \tag{2}$$

$$\frac{\partial h}{\partial t} + \vec{V}\cdot\nabla h = \frac{1}{\rho}\nabla.(K\nabla T) + \dot{h}_s \tag{3}$$

$$\dot{F}_s = \frac{\partial F}{\partial t} + \nabla\left(\vec{V}F\right) \tag{4}$$

where $\dot{m}_s$ is a term of external mass source, G_b is the acceleration due to body forces, $\vec{V}_s$ is the velocity vector of the mass source, and the term of $k_d\vec{V}$ represents the flow losses in the porous media model [31]. Concerning non-isothermal phase change, the latent heat of fusion is considered for the enthalpy between the solidus and liquidus temperature, as shown in Eq. (5).

$$h = \begin{cases} C_s T & T \le T_s \\ h(T_s) + L_f \frac{T - T_s}{T_l - T_s} & T_s < T \le T_l \\ h(T_l) + C_l(T - T_l) & T_l \le T \end{cases} \tag{5}$$

By neglecting the volume change (approximately 5%) that occurs with the phase transformation [32], the porous media drag concept is used for modeling the flow in the mushy zone according to Eq. (6) [31].

$$k_d = s_d \cdot \frac{f_s^2}{(1 - f_s)^3} \tag{6}$$

3.2. Boundary conditions and body forces

The surface of the workpiece is exposed to TP-GMAW heat sources in addition to the convection and radiation heat losses. For a TP-GMAW process with trailing and leading heat sources, the mathematical expression of heat flux at the surface is given as follows:

$$K\frac{\partial T}{\partial \vec{n}} = q_{trail} + q_{lead} - q_{rad.} - q_{conv.} \tag{7}$$

$$q_{rad.} = \varepsilon e_{S-B}\left(T^4 - T_0^4\right) \tag{8}$$

$$q_{conv.} = h_c(T - T_0) \tag{9}$$

Considering the efficiency of the GMAW process, the heat rate of each source is assumed to be equal to the sum of the arc heat rate and the droplets heat content as follows:

$$\eta Q = \eta\left(Q_{arc} + Q_{drop}\right) \rightarrow \eta\overline{UI} = \eta(1 - \eta_d)\overline{UI} + \eta\eta_d\overline{UI} \tag{10}$$

where the $\overline{UI}$ is the instantaneous average power [33], η is the welding efficiency and the η_d represents the ratio of the droplet heat rate and average power [34]. To compute the ideal amount of heat energy transferred by the droplets to the workpiece, the

Table 3
Symbols of mathematical formulation.

Symbol	Nomenclature	Symbol	Nomenclature
C_l	Specific heat capacity[†] (liquidus, J/kg K)	t	Time (s)
C_s	Specific heat capacity[†] (solidus, J/kg K)	T_d	Droplet temperature (K)
d_t	Surface tangential direction (m)	T_l	Liquidus temperature (K)
e_{S-B}	Stefan-Boltzmann constant (W/m^2 K^4)	T_m	Melting temperature of pure iron (K)
f_s	Local solid fraction	T_0	Ambient temperature (K)
f_d	Frequency of droplet generation (Hz)	T_s	Solidus temperature (K)
F	Volume fraction of fluid	U	Welding voltage (V)
$\dot{F}_s$	Change of F with the mass source	$\vec{V}$	Velocity vector (m/s)
F_a	Magnitude of arc force (N)	$\vec{V}_s$	Mass source velocity vector (m/s)
$\vec{g}$	Earth gravity vector (m/s^2)	$\vec{V}_n$	Normal velocity vector (m/s)
G_b	Total body force acceleration (m/s^2)	$\vec{V}_t$	Tangential velocity vector (m/s)
G_{2D}	Function of two-dimension drag force		
h	Enthalpy (J/kg)	*Greek symbol*	
$\dot{h}_s$	Enthalpy source of droplet (W/kg)	Γ_s	Surface excess at saturation (mol/m^2)
h_c	Convection coefficient (W/m^2 K)	γ	Surface tension (N/m)
I	Welding current (A)	γ_m°	Surface tension of pure iron (N/m)
k_1	Entropy factor	ΔH°	Heat of adsorption (J/mol)
k_d	Drag coefficient in porous model (1/s)	ε	Emissivity of the workpiece surface
K	Thermal conductivity[†] (W/m K)	η	Arc thermal efficiency
L_f	Latent heat of fusion (J/kg)	η_d	Droplet thermal power per total arc power
$\dot{m}_s$	Droplet mass source (kg/ m^3 s)	μ	Dynamic viscosity of fluid[†] (kg/m s)
$\vec{n}$	Normal vector of free surface	μ_p	Dynamic viscosity of plasma (kg/m s)
P	Pressure (Pa)	μ_m	Magnetic permeability of material (H/m)
Q	Heat power (J/s)	v_p	Plasma initial velocity (m/s)
r_d	Initial radius of the droplet (m)	ξ	Arc concentration coefficient
R	Gas constant (J/mol K)	ρ	Density of fluid[†] (kg/m^3)
Re_p	Plasma Reynolds number	ρ_p	Density of plasma (kg/m^3)
R_x, R_y	Curvature radii in x and y axes (m)	ρ_s, ρ_l	Density of solid and liquid[†] (kg/m^3)
s_d	Drag coefficient constant (1/s)	τ	Shear stress (Pa)

[g] Temperature dependent

equation of specific heat capacity is employed according to the frequency of droplet generation, f_d, in spray mode:

$$Q_{drop} = \frac{4}{3}\pi r_d^3 f_d \left\{ \rho_l C_l (T_d - T_l) + \rho L_f + \rho_s C_s (T_s - T_0) \right\} \tag{11}$$

As a key point of heat flux modeling, the part of heat, which is transferred by the droplets, must be deducted from the total heat. The heat flux on the free surface is modeled as a double-ellipse distribution by modification of the fixed Gaussian relation with effective radii in the front of the x direction (σ_{qxf}), the rear of the x direction (σ_{qxr}), and the y direction (σ_{qy}) [16,35]:

$$q_{arc} = \frac{\eta(1-\eta_d)UI}{\xi\pi\sigma_{q\bar{x}}\sigma_{qy}} exp\left\{ -\frac{(x - x_c - V_w t)^2}{\xi\sigma_{qx}^2} - \frac{(y - y_c)^2}{\xi\sigma_{qy}^2} \right\} \tag{12}$$

$$\sigma_{qx(trail\ )} = \begin{cases} \sigma_{qxf}, & x \geq x_c - V_w t \\ \sigma_{qxr}, & x < x_c - V_w t \end{cases}, \quad \sigma_{q\bar{x}} = \left(\frac{\sigma_{qxf} + \sigma_{qxr}}{2} \right) \tag{13}$$

where the x_c and y_c are the moving coordinates of the arc center and the V_w represents the welding velocity. Note that the leading and trailing electrodes follow the reverse suffixes in the front and the rear of x direction. The top surface of the molten pool interacts with the stress caused by the arc pressure and the plasma jet during welding. The pressure gradients produced by the electromagnetic force of the arc plasma create a downward stream of ionized gas along the normal of the free surface. Besides, impinging of the plasma jet on the free surface creates an outward flow in the weld pool. The pressure boundary condition in the presence of surface tension using Newton's viscosity [14] law is expressed as follows:

$$-P + 2\mu \frac{\partial \vec{V}_n}{\partial \vec{n}} = -(P_{arc.trail} + P_{arc.lead.}) + \gamma \left\{ \frac{1}{R_x} + \frac{1}{R_y} \right\} \tag{14}$$

where, P_{arc}, and γ are the pressure of free surface in the normal direction, the arc pressure, and the surface tension, respectively. The arc pressure in this study is assumed to have a double-ellipse distribution, where the magnitude and the effective radii are based on empirical measurement [36].

$$P_{arc} = \frac{F_a}{\xi\pi\sigma_{a\bar{x}}\sigma_{ay}} exp\left\{ -\frac{(x - x_c - V_w t)^2}{\xi\sigma_{ax}^2} - \frac{(y - y_c)^2}{\xi\sigma_{ay}^2} \right\} \tag{15}$$

$$\sigma_{ax(trail\ )} = \begin{cases} \sigma_{axf}, & x \geq x_c - V_w t \\ \sigma_{axr}, & x < x_c - V_w t \end{cases}, \quad \sigma_{a\bar{x}} = \left(\frac{\sigma_{axf} + \sigma_{axr}}{2} \right) \tag{16}$$

where the σ_{axf}, σ_{axr}, and σ_{ay} are the effective radii of the arc pressure in the front x direction, rear x direction, and the y direction, respectively. The plasma jet shear on the free surface of the weld pool is defined by an analytical solution [37] in terms of Reynolds number, jet height, and the nozzle diameter.

$$\frac{\tau}{\rho_p v_p^2} Re_p^{1/2} (H/D)^2 = G_{2D}(r/H) \tag{17}$$

The arc length and the filler diameter are supposed to be the jet height (H), and the nozzle diameter (D), respectively, while the symbol r refers to the radial distance from the center. The velocity of the jet and the plasma Reynolds number are computed by the maximum arc pressure at the center of the weld pool based on Bernoulli's equation:

$$v_p = \sqrt{\frac{2P_{arc@center}}{\rho_p}} \rightarrow Re_p = \frac{D}{\mu_p}\sqrt{\frac{2\rho_p F_a}{\xi\pi\sigma_{a\bar{x}}\sigma_{ay}}} \tag{18}$$

To investigate the Marangoni shear with accuracy, the surface tension is modeled in terms of temperature and the surface-active elements. Sahoo et al. [26] approximated the surface tension relation of a pseudo-binary Fe–S system as a function of both temperature and the activity as follows:

$$\gamma = \gamma_m^\circ - A(T - T_m) - RT\Gamma_s ln\left[1 + k_1 a_s e^{-(\Delta H^\circ/RT)}\right] \tag{19}$$

Note that the activity of sulfur (a_s) considered equal to the wt% of the content and the symbol A corresponds to a negative gradient of surface tension for the pure iron. Due to the high amount of manganese and silicon in the filler composition and their deoxidant [38], the effect of oxygen on the gradient of surface tension is ignored in this simulation. The change in surface tension with the temperature and the induced shear stress are balanced on the free surface following the Eq. (20):

$$\mu \frac{\partial \vec{V}_t}{\partial \vec{n}} = -\frac{\partial \gamma}{\partial T}\frac{\partial T}{\partial d_t} \tag{20}$$

The vibration momentum is another boundary condition applied in this investigation to incorporate the vibration of the workpiece during welding. The displacement (x_l), instant velocity (v), and peak acceleration (G_p) of the workpiece for a given frequency of sinusoidal vibration can be expressed as:

$$x_l = (D/2)\sin(2\pi f t) \tag{21}$$

$$v = D\pi f \cos(2\pi f t) \tag{22}$$

$$|G_p| = 2D(\pi f)^2 \tag{23}$$

where D is the peak to peak displacement,f is the frequency of vibration, and G represents the acceleration, respectively. The acceleration reaches a peak (G_p) when $\sin(2\pi f t) = 1$, as shown in Eq. (23). Applying the vibration as fixed acceleration leads to continuous change in velocity at the boundary and subsequently in the whole weld pool. The effect of vibration on the molten pool is investigated during the simulation. The body forces, including the electromagnetic (Lorenz) and the buoyancy, are adopted as the term G_b in the Navier–Stokes equation (Eq. (2)). The components of body forces for a tandem wire in the Cartesian coordinates are defined in the following form:

$$\vec{F} = \left(\vec{J_1} \times \vec{B_1}\right) + \left(\vec{J_2} \times \vec{B_2}\right) - \rho\vec{g}\beta_t (T - T_l) \tag{24}$$

where $\vec{J}$ and $\vec{B}$ are the current density and the magnetic field vectors. The third terms of Eq. (24) represents the buoyancy force concerning the negative z direction assumed for the gravity and the thermal expansion coefficient (β_t) computed using the density variation caused by temperature. Due to the pulse welding and the fluctuation of both the free surface and current flow, the simplified model of electromagnetic force [39] in double-ellipse mode is used in this simulation (Eq. (25)). To increase the accuracy of the simplified model, an additional factor, β, is incorporated based on Kumar and DebRoy [40].

$$\left(\vec{J} \times \vec{B}\right) = \left\{ \frac{-\mu_m I^2}{2\xi\pi^2 r\sigma_{ex}\sigma_{ey}} \exp(\varphi) \times [1 - \exp(\varphi)]\left(1 - \frac{Z_s - Z}{L}\right)^2 \right\} \times \left\{ \frac{(x - x_c - V_w t)}{r}\vec{i} + \frac{(y - y_c)}{r}\vec{j} \right\} + \left\{ \frac{\beta\mu_m I^2}{2\xi r^2\pi^2 L}[1 - \exp(\varphi)]^2\left(1 - \frac{Z_s - Z}{L}\right) \right\}\vec{k} \tag{25}$$

$$r = \sqrt{(x - x_c - V_w t)^2 + (y - y_c)^2}, \tag{26}$$

$$\varphi = -\frac{(x - x_c - V_w t)^2}{\xi\sigma_{ex}^2} - \frac{(y - y_c)^2}{\xi\sigma_{ey}^2}, \tag{27}$$

$$\sigma_{ex(trail\ )} = \begin{cases} \sigma_{exf}, & x \geq x_c - V_w t \\ \sigma_{exr}, & x < x_c - V_w t \end{cases}, \quad \sigma_{e\bar{x}} = \left(\frac{\sigma_{exf} + \sigma_{exr}}{2} \right) \tag{28}$$

where the σ_{exf}, σ_{exr}, σ_{ey}, and Z_s are the effective radii of the electromagnetic force in the front x direction, rear x direction, y direction, and the vertical position of the free surface, respectively.

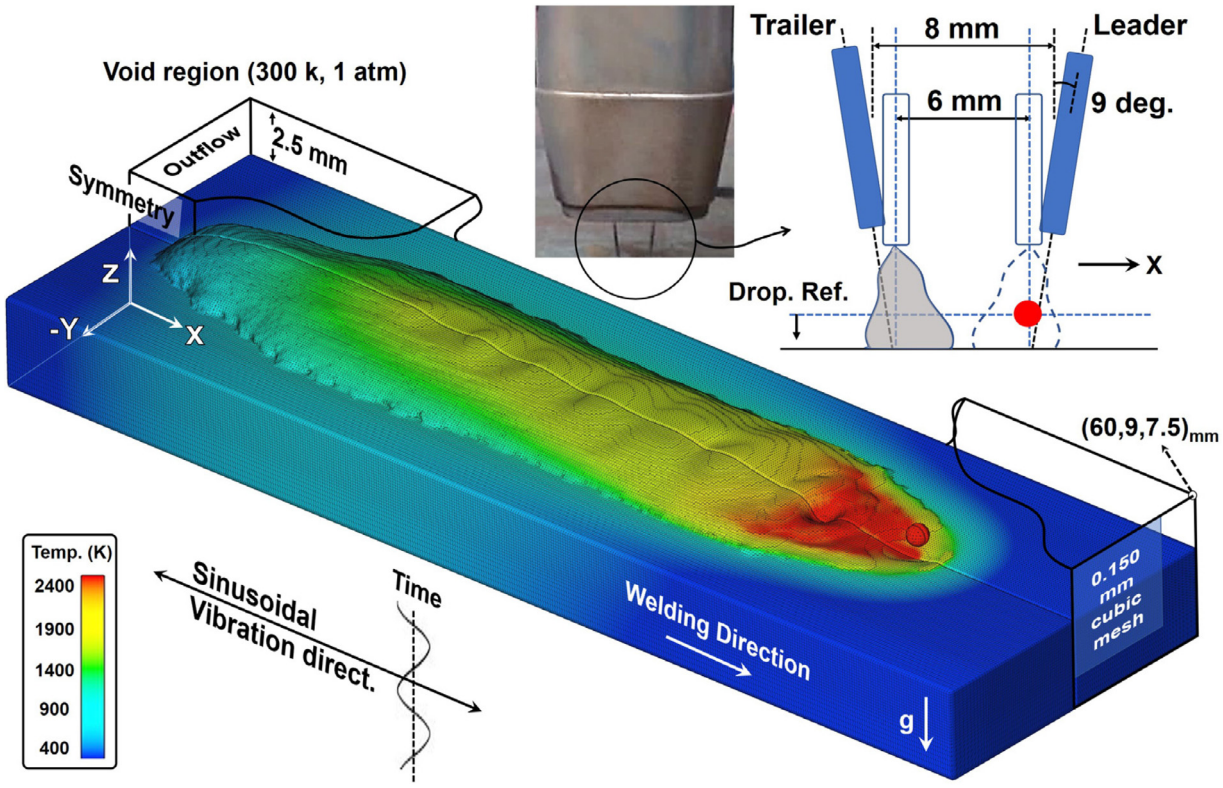

Fig. 3. The computational domain and the coordinates used for half symmetry of CFD simulation.

3.3. Numerical process and consideration

The computational domain (i.e., workpiece) is divided into two regions, void, and fluid, where the void properties are considered like the ambient air. Since a single fluid is used in the model, the solid and liquid phases are distinguished based on the enthalpy-temperature relationship (Eq. (5)). At the start of the simulation, the computational domain of 60 × 9 × 7.5 is assumed to be the solid phase (pseudo fluid under the melting temperature) of 5 mm thickness and 2.5 mm thickness of the void, as shown in Fig. 3. The fluid temperature of each cell is determined from its enthalpy, which is computed based on conduction and convection of material. Cho et al. [15] utilized a 0.25 mm cubic mesh size as the proper mesh-independent domain to satisfy the total accuracy. Despite a good resolution on the spot-welding profile and fair agreement with the experimental result on the stationary GMAW, it is not adequate to produce a clear penetration of the fusion zone, as desired in this investigation. Therefore, the computational domain, meshed by 0.15 mm of the cubic cells at the center and a maximum 0.2 mm in the surrounding, is considered to simulate only half of the weld pool in symmetric coordinates. The graphical schematic of the simulation domain is shown in Fig. 3. The arc interaction is simplified to only two current conditions: pulse-background and background-pulse. The intermediate effect of arc interaction fairly is ignored in simulation because of 2.2 ms delay between pulse-charging and very short time of overlapping. The wire speed, torch angle, and the arc interaction affect the droplet path while falling and impinging at a relatively closer position in comparison to the initial state of two sources [41]. On the other side, to control the droplets movements and reducing the errors, it is assumed that the spherical droplets generate at 1.5 mm above the top surface. This assumption makes an important deviation from the real condition of welding in addition to other minor effects. Consequently, two parallel sources are assumed in a close distance, 6 mm, versus an initial 8 mm to improve the simulation accuracy. The 6 mm distance is obtained through experiments wherein the torch rotates 90 degrees along the Z axes keeping other conditions same. Both sources travel in the X direction with a constant velocity of 1.2 m/min. The initial radius of droplets, 0.59 mm, is estimated by the mass balance of droplet generation frequency and the electrode feed rate. The generation frequency follows the current pulse frequency, which means one drop per pulse is produced in a quasi-stable condition of the spray mode with respect to shielding gas [42]. The metal evaporation is neglected because of the maximum temperature in the model remain below the boiling temperature (2900 K) during welding. The temperature and initial velocity of the droplet are set to 2500 K and 0.7 m/s, respectively, for without (W/O) vibration case [16,43].

Employing the liquid nitrogen calorimetry, the total efficiency of energy in P-GMAW was measured by Joseph et al. [33] with a range from 67% to 72%. In this study, the total efficiency of 68% is adopted for the GMAW process. The ratio of the droplet heat rate per average power is obtained 36% and consequently, the arc heat efficiency ($\eta(1-\eta_d)$) and droplet efficiency ($\eta\eta_d$) are estimated 43.5% and 24.5%, respectively. The efficiency results are in agreement with previous study [44]. Analysis of the current values revealed a decrease in both background and the pulse current by applying the vibration. The similar results are obtained for voltage values. For the purpose of calculating the heat rate in Eq. (10), the average current, is chosen based on the histogram of the values recorded during an intermediate duration of welding (5 to 7 s), as illustrated in Fig. 4. Reduction of heat input affects the initial temperature of the droplet in addition to the change in the dynamic balance of the weld pool. The initial droplet temperature, 2400 K, in the presence of vibration is estimated by Eqs. (10) and (11) assuming that the efficiency values are fixed for both with and without vibration cases. The voltage varies from 25 to 39 V for which the arc length of each electrode in the stable condition is set to 4.8 mm [15].

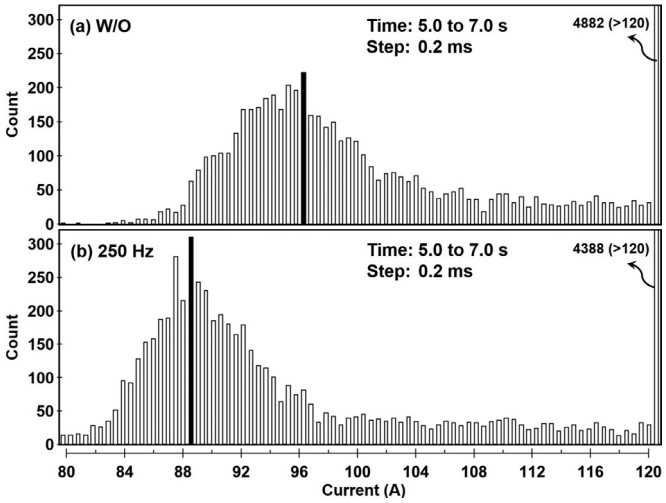

Fig. 4. The histogram of welding current in the background range of (a) W/O vibration and (b) 250 Hz of vibration.

The effective radius of the electromagnetic force as the function of the current is estimated by the empirical relation extracted from the results of Tsai and Eagar [45]:

$$\sigma_e = 7.209 \times 10^{-4} \times I^{0.2288} \tag{29}$$

To calculate the double-ellipse effective radii based on the Gaussian radii (Eq. (29)), the arc interaction phenomenon is employed from the previous study [41]. Using the current values of the leading electrode at the background and the trailing at pulsed mode, 96 and 330 A, respectively, the deflection of the pulsed arc is estimated at 0.56 mm. With the combination of effective Gaussian radii in the pulsed mode and the deflection value, the relation between the effective parameters can be approximated as follows:

$$\sigma_{e(Trail)} = \begin{cases} 0.83\sigma_{exf} \\ 1.26\sigma_{exr} \\ 1.26\sigma_{ey} \end{cases}, \quad \sigma_{e(Lead)} = \begin{cases} 1.26\sigma_{exf} \\ 0.83\sigma_{exr} \\ 1.26\sigma_{ey} \end{cases} \tag{30}$$

As discussed above, the intermediate arc interaction is ignored due to the simplification of the model and the lower value of current in the background. Also, the effect of arc deflection on the longitudinal movement of droplets during travelling to the molten pool is considered as the fixed value by defining the specific coordinate for the droplet sources. The enhancement factor in the Eq. (25), β, increases parabolically from 1 at 1 mm below the surface to 4 at the free surface. The thickness of the workspace (L) is set to 10 mm equal to the thickness of the welding plate, which is independent of the thickness of the simulation domain. In this study, it is assumed the effective radii of heat and arc pressure follow the equivalent factor of Eq. (30) in double-ellipse mode. The effective radius of Gaussian heat for a 4.8 mm arc length was estimated based on the empirical equation as a function of current in SI units [45]

$$\sigma_q = 6.205 \times 10^{-4} \times I^{0.28} \tag{31}$$

The arc force and the effective radius of the arc is calculated according to the experimental result of the previous investigations [36,46]

$$F_a = -4.307 \times 10^{-2} + 1.981 \times 10^{-4} \times I, \; I > 218\,A \tag{32}$$

$$\sigma_a = 1.404 \times 10^{-3} + 1.740 \times 10^{-6} \times I \tag{33}$$

These relations were estimated by 90° tip angle of the electrode. Despite the total arc force in the gas tungsten arc welding is a function of the square of the current, in the GMAW with limited range of effective current (on the arc pressure) the total arc force can be extrapolated by a linear function of current as reported by Zhang et al. [36]. Phares et al. [37] estimated the plasma shear distribution based on variation in H/D in two-dimensional conditions. The result was extrapolated by Cheon et al. [21] in the form of exponential functions and employed in this study by a minor modification:

For $H/D = 4$:

$$G_{2D}(r/H) = -22.28 \times \exp\left[-\{(r/H + 0.0451)/0.115\}^2\right] + 4.20 \times 10^{15} \times \exp\left[-\{(r/H + 34.34)/5.978\}^2\right] \tag{34}$$

Table 4
Thermophysical properties of IS2062 and the welding environment.

Property	*Value*
Ambient and the base metal initial temperature	300 K
Arc concentration coefficient	2
Convection coefficient	100 W/m^2 K
Density of plasma argon (10,000 K, 1 atm)	4.6 × 10^{-2} kg/m^3
Drag coefficient constant	1 1/s
Emissivity of weld metal	0.5
Gas constant	8.314 J/mol K
Liquidus temperature	1778 K
Latent heat of phase change (fusion)	2.75 × 10^5 J/kg
Magnetic permeability of material	1.26 × 10^{-6} H/m
Maximum plasma arc pressure (at 330 A)	908 Pa
Solidus temperature	1698 K
Stefan–Boltzmann constant	5.67 × 10^{-8} W/m^2 K^4
Viscosity of plasma argon (10,000 k)	5 × 10^{-5} kg/m s

The thermophysical properties of IS2062 steel applied in this simulation are shown in Table 4. The phase transformation and the effect of alloy elements on the different physical properties are considered in temperature-dependent conditions (Fig. 5). The properties are collected from the different databases, including the fluid database of FLOW-3D and the other literature on the low carbon steels [31,47]. The surface tension of the free surface is defined as a function of both temperature and the sulfur content in a pseudo-binary Fe–S system [26]:

$$\gamma = 1.943 - 4.3 \times 10^{-4}(T - T_m) - RT \times 1.3 \times 10^{-5} \times ln\left[1 + 0.00318 a_s e^{(1.66 \times 10^5/RT)}\right] \tag{35}$$

The gradient of surface tension changes its sign from negative at higher temperatures to positive at lower temperatures, as shown in Fig. 6. The sulfur content can be approximated in terms of dilution that is obtained about 44% in both cases. In the present study, the average sulfur of 0.028 wt% is considered that corresponds to the base metal and the filler material content, 0.018 and 0.035 wt%, respectively. The importance of transient temperature and the Marangoni flow is illustrated in Fig. 6(b).

The vibration frequency of 250 Hz at a fixed acceleration of 1.2 m/s^2 is applied to the workpiece. The velocity of sinusoidal vibration changes continuously from 0.764 mm/s to −0.764 mm/s in the X-direction. For more accurate tracking of fluid, the split Lagrangian VOF method is employed with the explicit solver for the viscous stress [20]. The generalized minimum residual (GMRES) method is used as the pressure-velocity solver. The maximum time step set to 10^{-5} s is limited by the convergence criteria of both advection and the surface tension. For generating the pulsed waveform following the recorded results, a trigonometric relationship is used as follows:

$$F(I,t) = I_1 + \frac{(I_2 - I_1)}{2}\left(1 + sin\left(\frac{2\pi}{P_d}t - \frac{\pi}{2}\right)\right) \tag{36}$$

where the I_1, I_2, and P_d are the background current, the pulsed current, and the pulse duty of total waveform, respectively. The simu-

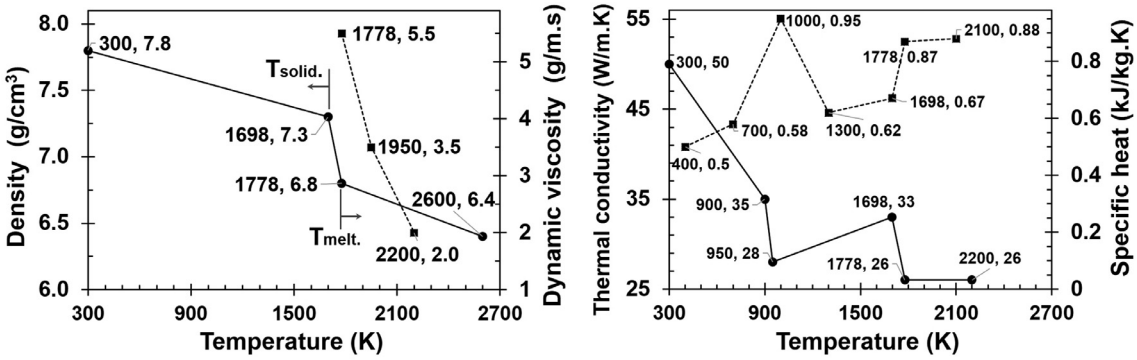

Fig. 5. The temperature-dependent physical properties of IS2062 steel.

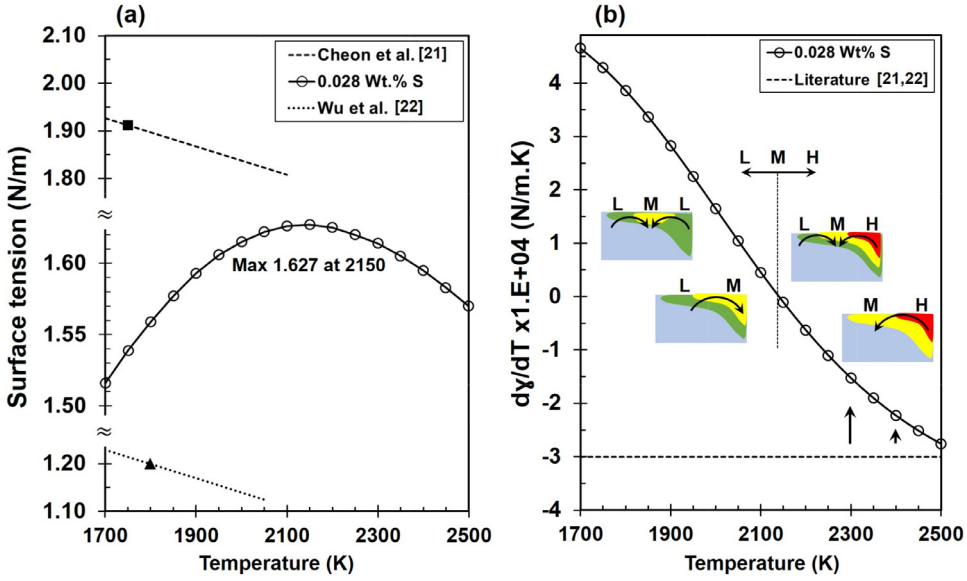

Fig. 6. The surface tension (a) and its gradient (b) as a function of temperature and sulfur wt%. Concerning the transition temperature in the mid-range (M), the high and low temperatures are marked with the letters H and L, respectively.

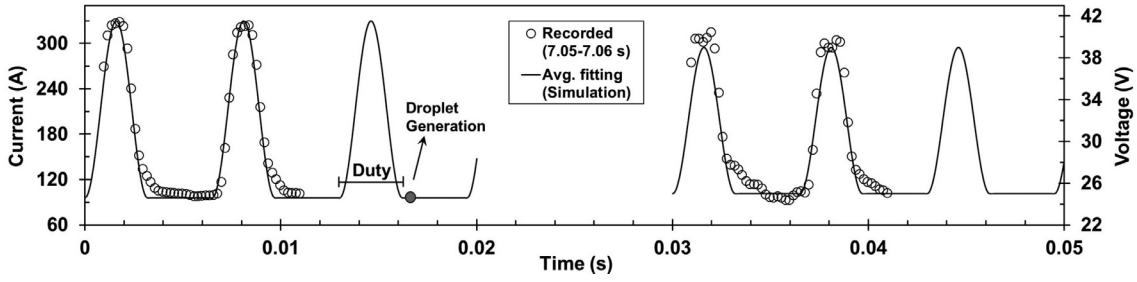

Fig. 7. Periodical change of the welding current and voltage, fit by trigonometric relation in W/O vibration.

lated waveforms for both current and voltage are shown in Fig. 7. The recorded average power per electrode, 4957 J/s, in comparison with the simulated average power 4740 J/s, confirms the accuracy of the model within 5% error. The droplets generation time is synchronized with the waveform once the pulse ends up at each cycle during the total simulation time.

4. Results and discussion

4.1. Validation of model by experimental results

The cross-sections of both with and without vibration experiments are employed to validate the simulation results. Due to the dynamic nature of the weld pool, the boundary of the fusion zone continuously changes from the droplet impingement to complete solidification. To evaluate the boundary, the solid fraction of the specific cross-section is extracted in the period and overlaid on a specific 2D image as a stroboscopic shot. The boundary of the solid fraction refers to the cells melted partially (mushy zones) by a ratio of 50%. The terms of period and references need to be discussed before analyzing the results. All partially melted cells represent the final boundary that can be seen in the OM images. However, it is found that the geometry of the melted boundary does not generate at an instance. Instead, at least two distinct times must be used for the prediction of the melted boundary in agreement with experimental results. The main reason for this phenomenon corresponds

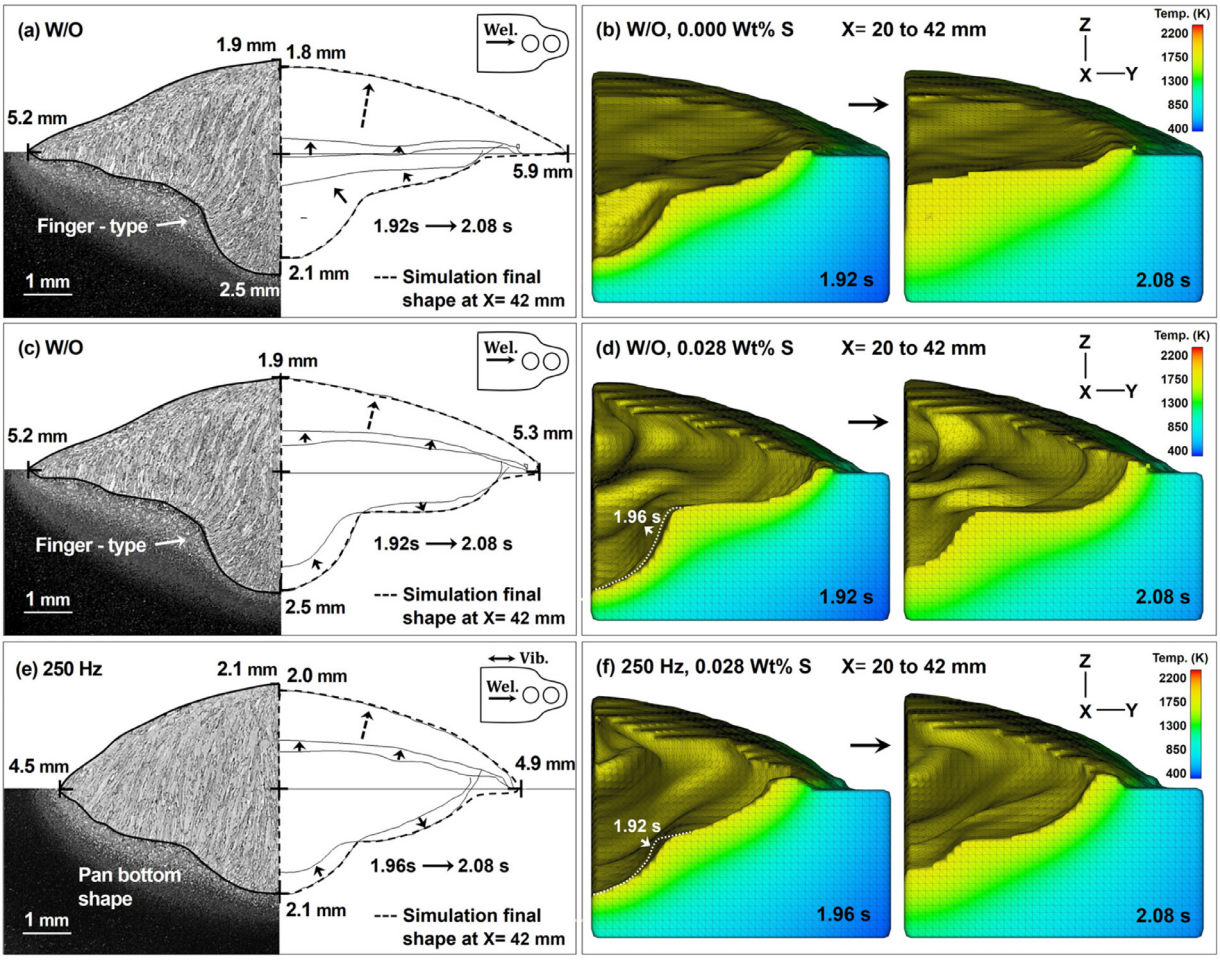

Fig. 8. The OM images from a cross-section of welding experiment and the corresponding simulation result in solid fraction mode: (a, b) W/O vibration and the simulated by ignoring the sulfur effect, (c, d) W/O vibration simulated by 0.028 wt% of sulfur and, (e, f) 250 Hz of vibration simulated by 0.028 wt% of sulfur content.

to the fluid flow of the molten pool in tandem wire welding. In the present study, the position of X=42 mm is chosen for the examination due to the stable behavior of the weld pool. The final height of the weld bead is estimated by the rear layer (X=20 mm) because of the limitation of both simulation time and domain dimension. Fig. 8 represents a comparison of the simulation results with the OM images (left half of Fig. 8a, c, and e) of the samples; W/O vibration and 250 Hz of vibration. As shown in Fig. 8(a) and (b), the simulation shows a shallow penetration in comparison to the experiment by ignoring the sulfur effect on the surface tension value and its gradient. Adding sulfur content to the simulation makes a more accurate prediction of the final geometry concerning the fluid flow effect on the melting of the weld toes and the depth of the weld pool, as shown in Fig. 8(c and d). By ignoring the sulfur content, the weld width in the Y direction is overpredicted by 13 % (Fig. 8a). The overprediction limits to 2% when the sulfur content is considered in the simulation (Fig. 8c). Similarly, underprediction of total weld height in Z direction comes down from 11% when sulfur content is ignored to <1% when the same is considered.

The existence of a specific pattern near the vertex of curvature and the bottom of the weld pool in the OM image support the concept of the different timing of solidification. The comparison of Fig. 8(d and f) reveals that the time needed for the creation of the final geometry in the presence of vibration is shorter than the W/O vibration case, despite the overlapping of many features of the welding conditions. This difference presents the importance of change in heat input, which is the consequence of applying the vibration. In summary, the simulation outcomes considering the effect of surface tension active element show a good agreement with the experimental results, with and without vibration. In the case of without vibration, the fusion zone dimensions follow the experiment, while the weld toes are overestimated. It is suggested that the simplified heat sources and the predefined contact angle of surface tension (90°) caused these differences. Material properties can explain the other reason based on the equilibrium phase diagram and the phase change effect because the rate of heating in the melting condition is higher than the equilibrium conditions.

4.2. The mechanism of finger-type penetration and the vibration effect

In tandem wire case, first, the droplets of the leading electrode impinge the workpiece and create a shallow melted zone corresponding to the welding speed. The procedure is followed by an increment of heat in the space between the two electrodes, and in the next step, deeper penetration is caused once the droplets of the trailing electrode strike the surface. Considering the time needed for the stable condition of welding, the depth of penetration at this stage is suggested to be equal to the final depth of the cross-sectional OM image due to the effect of the heat transfer from the superheated metal of droplets into the weld pool. However, the geometry of the weld pool, including the width and the penetration shape cannot be explained by only the heat distribution in the tandem welding. The arc interaction phenomena and

the sulfur content of filler material in tandem welding affect the weld pool geometry from a different point of view. The surface area under the leading electrode, as the highest temperature zones, determines the final shape of the weld pool based on the balance between temperature-dependent forces and the other body forces. The surface-active solute systems under the welding conditions were studied previously from the thermodynamic viewpoint [48] and can be applied to this discussion. The negative gradient of surface tension naturally creates an outward flow to the weld toes, where the high temperature near the droplet temperature is maintained. The interaction between the impact acceleration of the droplets, the inward electromagnetic force, and the negative surface tension gradient at the weld pool creates the finger-type penetration at this step. As a result, the cross-section includes a very strong downward flow at the center and a weak outward flow at the toes. Before discussing the controlling mechanism of surface tension, the longitudinal flow must be considered here.

In addition to all the forces that act on welding, the electrodes' movement, and the droplet impingement create a long-term flow of material in the longitudinal section. Because of this cycle, the part of the material that has not been solidified returns from the upper half of the longitudinal cross-section and move to near the trailing electrode. This flow of material feeds the weld toe in the cross-section, besides, to participate in longitudinal cycling [21]. With this explanation, the surface tension gradient can strengthen the outward flow towards the weld toes near the electrode. By moving away from the trailing electrode and decreasing the effect of electromagnetic and the other centralized forces, the surface tension gradient can dominantly control the geometry of the weld pool. However, the surface tension itself is controlled by temperature, and thus the positive gradient enhances the downward flow at the center or toes depending on the position with higher temperature. The positive gradient forms the final shape of weld toes since the center of the molten pool, in the presence of the longitudinal molten cycle, needs more energy than toes to change without the support of the other forces. The other important part of this scenario is the effect of the transition temperature of the surface tension gradient. With respect to the estimated transition temperature, 2150 K, in this study, and the higher values of temperature below the trailing arc, the positive gradient is unable to act and change the penetration depth. Here the effect of sulfur content on the negative gradient must be considered. Despite the existence of a negative gradient of surface tension at a higher temperature and the presence of surface tension active element, the intensity of the outward flow reduces in comparison to the outward flow in low sulfur Fe–C alloys. As a result, shallow penetration occurs because of neglecting the effect of sulfur concentration. It must be noted that the specific condition of tandem welding itself produces deeper finger-type penetration in comparison to the single wire as discussed before. By increasing the sulfur concentration at the surface, the transition temperature shifts to higher values [28]. This increment reduces the outward flow under the trailing electrode and in the following makes a downward force at high-temperature zones when the temperature drop from transient value, finally leads to more centralized geometry. Although the transition temperature of surface tension severely affects the final penetration shape, the instantaneous gradient value also plays its role partly.

By specifying all the preconditions, the vibration effect based on the simulation results can be discussed. Fig. 9 shows the temperature distribution of free surface from top view in both W/O vibration and 250 Hz of vibration at 1.96 s. Based on the results, the heat on the free surface expands along the welding direction in the presence of vibration. As it is mentioned previously,

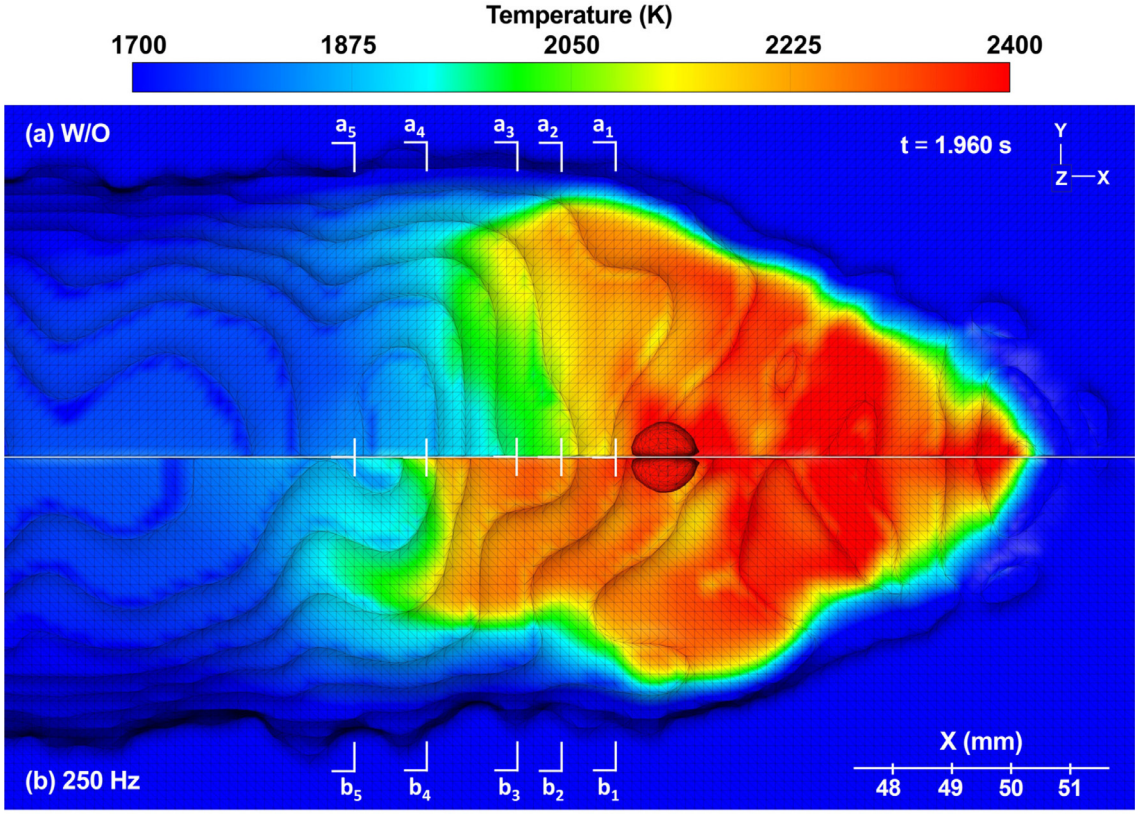

Fig. 9. The temperature distribution of free surface at both W/O vibration and 250 Hz of vibration at 1.96 s. The marked a_1 to a_5 and b_1 to b_5 are the position of the cross-section chosen to analyze the streamlines in Fig. 10.

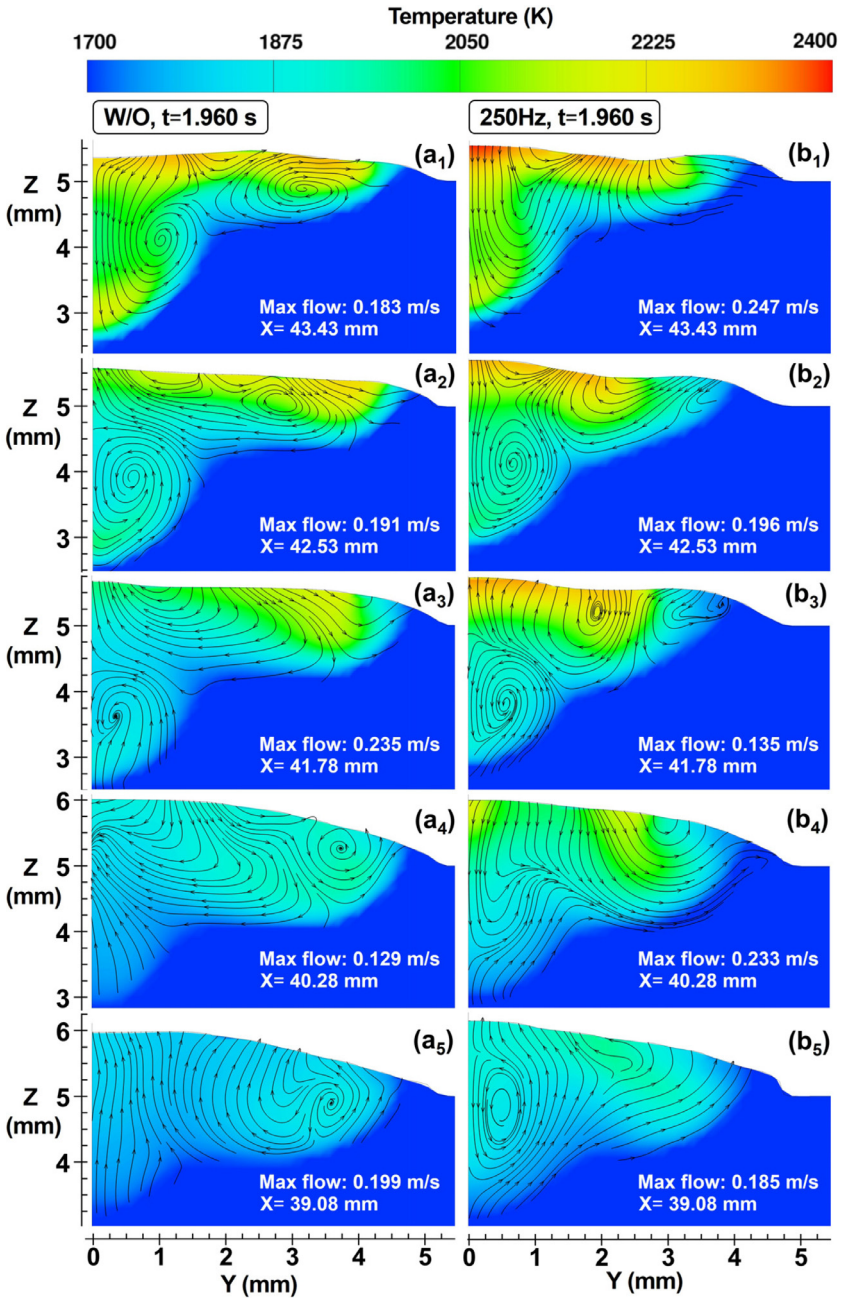

Fig. 10. The streamlines and the temperature variation in *X*-planes at 1.96 s. The W/O vibration and the 250 Hz of vibration samples marked by a_1 to a_5 and b_1 to b_5, respectively.

applying the vibration decreases the heat input of welding. However, the longitudinal heat expanding in the vibration direction is good evidence of the physical effect of vibration. The cross-sectional images from the rear of the trailing electrode are used to visualize how the Marangoni effect controls this region dominantly and affects the penetration shape. Fig. 10 illustrates the five cross-sections captured at the time of 1.96 s simultaneously. In a steady-state condition, there is a possibility to track the paths of the massless fluid element by placing streamlines at an arbitrary location to illustrate the nature of the vector field flow [49].

Assuming that the vector field represents the velocity of the fluid and the streamlines in Figs. 10 to 13 are instantaneously tangent to the velocity vectors help to interpret the results. The area near the droplet impingement is still controlled by inward forces such as droplet impact momentum and electromagnetic force. Fig. 10(a_1) and (b_1) shows an inward flow because of higher droplet temperature. Higher heat flux in W/O vibration case makes a deeper penetration from an early stage. Nevertheless, the central surface area in 250 Hz sample preserves the high temperature for a longer period. The surface temperatures at a_1 and a_2 are higher than the transition temperature (2150 K) that results in a negative gradient of surface tension that, in turn, creates a flow from high to low-temperature region. This mechanism remains valid until the temperature drops from transition temperature, and the reverse flow is activated.

The interaction of the buoyancy force and the Marangoni flow would lead to the eddies at weld toe of a_1. In contrary to the W/O vibration, any kind of eddy is not observed at b_1 probably because of the dominant flow perpendicular to the cross-section. By moving away from the position of trail electrode, the fluid follows

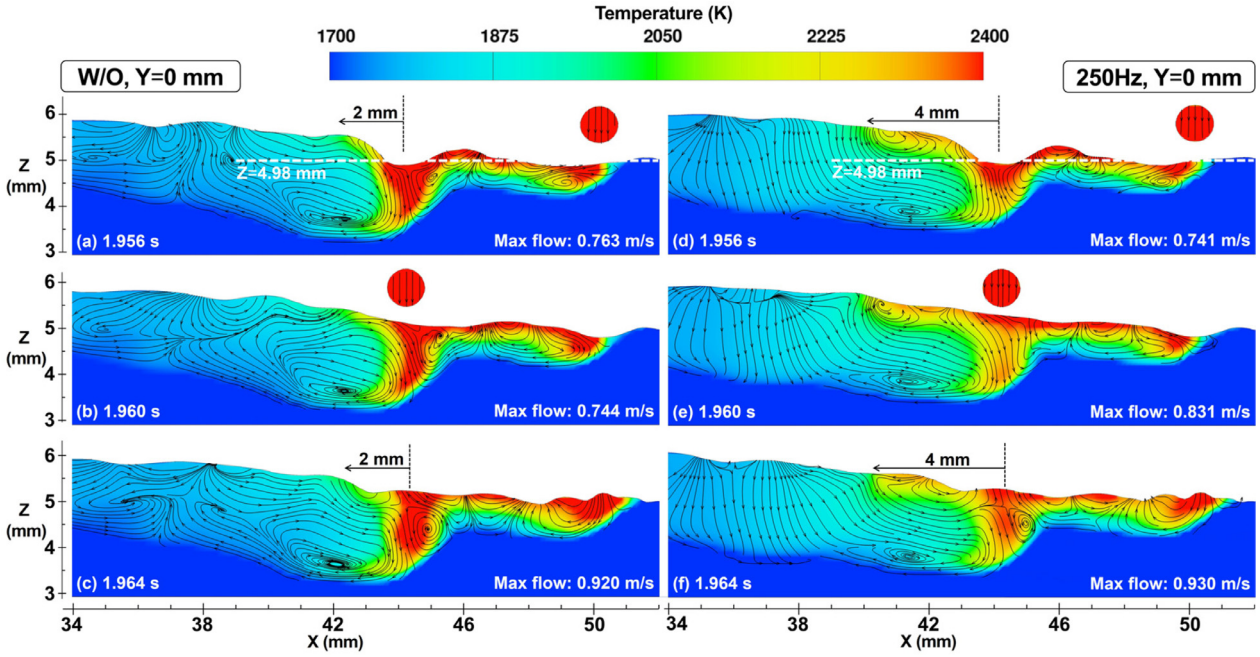

Fig. 11. The streamlines and the temperature color map of the central *Y*-plane from 1.956 to 1.964 s of simulation time.

different patterns in W/O vibration and 250 Hz cases. The position a_2 and a_3 (Fig. 9) in W/O vibration show the LML pattern (see Fig. 6b) towards the weld toes while the corresponding figures of 250 Hz, b_2 and b_3, represent the HML pattern towards the depth of weld pool. Note that the weld pool dynamics can affect the streamlines and make a deviation from the ideal pattern of the Marangoni effect.

The enhancement of material flow towards the weld toes at a_3 melts the side boundaries without affecting the angle of curvature and produces a finger-type penetration. The bottom eddy at b_2 and b_3 is actively fed by droplet momentum and the main longitudinal cycle. Interaction between the HML type of Marangoni pattern towards the depth of the weld pool and the bottom eddy lead to melting of the vertex of the curvature and create a pan bottom penetration. This change is equivalent to what happened in a fixed position, 42 mm, from 1.92 to 1.96 s (see Fig. 8f). The mentioned mechanism clearly distinguishes the movement of boundaries in both cases. Despite the bottom of the cross-sections at a_4 and b_4 is charged by the droplet content from the front layer and are almost similar, the central area of the weld pool shows the different paths of material flow. In image a_4 in Fig. 10, the fluid returns near to the surface, but this path tends to the side of the weld pool in b_4 image. The other differences include the downward path of material in the central area from the surface and the noticeable higher velocity in the side of b_4 image induced by a positive gradient of surface tension. The images a_5 and b_5 show the solidified boundary moving gradually near to the surface. At the same time, the solidification at the bottom of a_5 occurs faster than b_5 due to expanded free surface and lower central temperature. Finally, comparison of a_5 and a_4 images reveal the effect of surface wave on the instantaneous height of cross-section that leads to the formation of ripples on the solidified surface of the weld [16].

4.3. The heat and material flow analysis of the tandem-GMAW process

The push-pull pattern on the surface of the molten pool between the two arcs and interaction with the surface tension gradient at the rear region make a very complex fluid flow through the weld pool. Supported by the fine mesh, different kinds of eddies can be observed for a short while. To distinguish the dominant and temporary flow patterns in the designated region, the stroboscopic images must be considered. Two sets of longitudinal cross-section images are employed to provide a continuous projection from the flow pattern in W/O vibration and 250 Hz of vibration, as shown in Fig. 11. The longitudinal cross-section confirms the expanded high-temperature region at the presence of vibration accompanying with the important detail of the major cycle of molten metal parallel to the welding direction. The large stable eddy exists at the bottom of the pool independent of the vibration effect. Despite the front area of the trail electrode shows almost similar flow patterns in both cases, the behind region follows distinct behavior. In W/O vibration sample, a long-term cycle expands to 37 mm of *X*-axis and returns to the upper level of the molten pool, as illustrated in Fig. 11(a–c). The corresponding time of current change is designated by a–c in Fig. 2. Except in Fig. 11(a) where the material comes to the free surface directly, in the other conditions (Fig. 11b and c), the material rises to half of the molten pool then returns to the front side. In the presence of vibration (Fig. 11d–f), it is obvious that the droplet content cannot return to the upper level of the pool from the center *Y* plane.

The rear region shows a dominantly downward stream in all the periods. As a result, the side planes ($Y<>0$) play a more important role in feeding the rear zone of the weld pool and keep the mass balanced during vibration-assisted welding. Fig. 12 represents the streamlines and the temperature color map of the workpiece surface plane from 1.956 to 1.964 s of welding. Similar to Fig. 11, the areas in the front of the trailing electrode ($X>44$ mm) show a very close pattern of streamlines in W/O vibration and 250 Hz of vibration. By moving to the rear region, the patterns are time-dependent, and thus, some short-range eddies or neutralized areas were appearing temporary. In W/O vibration images, Fig. 12(a–c), the aligned streams bring the material from the side of weld pool to the center zone around 40 mm of *X*-axis, while the corresponding area in 250 Hz, d to f, shows the opposite direction of the material flow. A comparison of the Figs. 10 and 12 proves the flow paths that occur at the free surface of the molten pool act differently from the internal layers such as Z=4.98 mm.

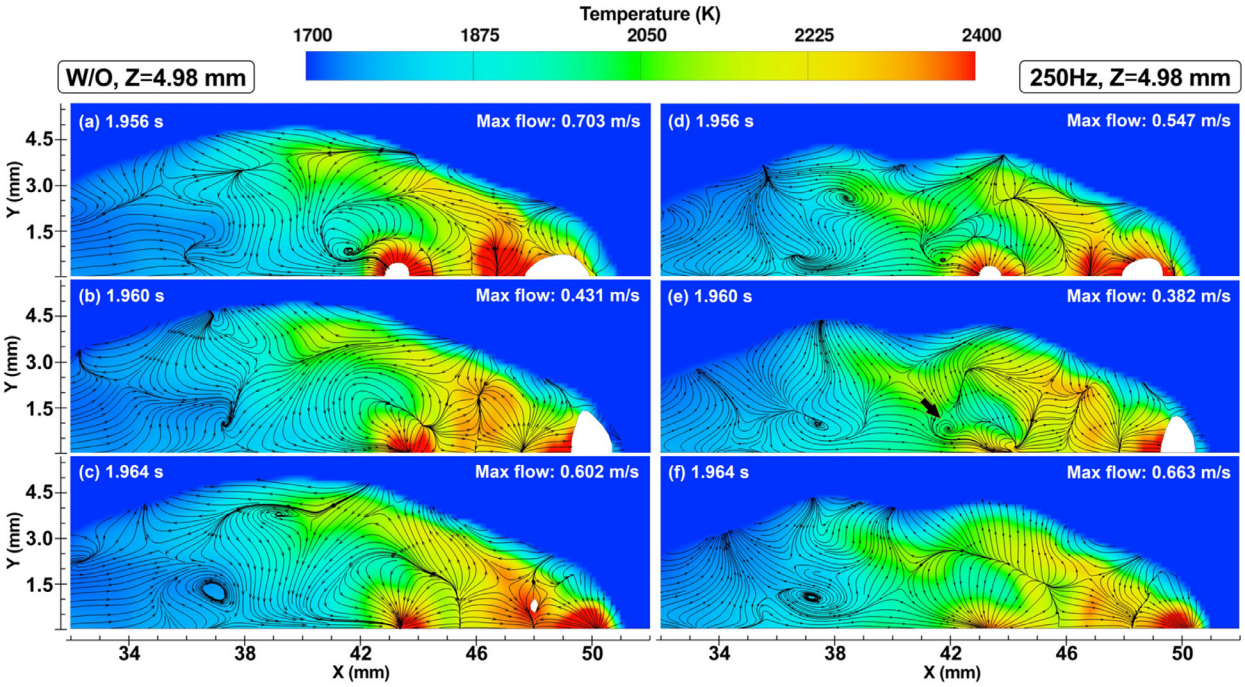

Fig. 12. The streamlines and the temperature color map of the Z=4.98 mm plane from 1.956 to 1.964 s of simulation time. The white zones represent the vacant area of the cross-section.

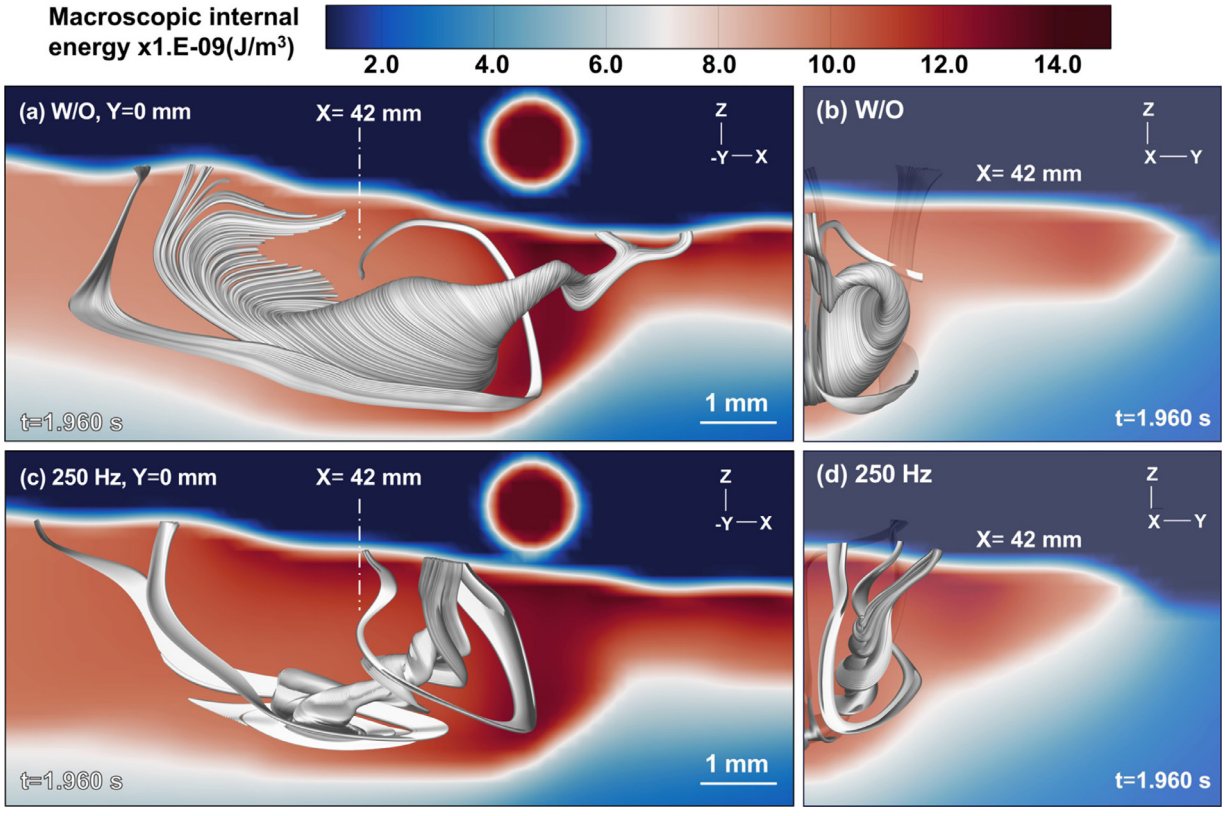

Fig. 13. The 3D streamlines plotted on the color map of internal energy at the Y=0 and X=42 planes by 1.960 s of simulation time. (a and b) represent the W/O vibration case while the c and d were corresponding to 250 Hz samples.

Three-dimensional (3D) streamlines can be used to show these kinds of sudden changes in addition to the dominant eddies. Fig. 13 demonstrates the series of 3D streamlines at 1.960 s of simulation time.

For better comparison, the central eddies are computed with similar references in the time scale. For better visualization, only the dominant eddies are shown in Fig. 13. In W/O vibration case, a large eddy can be seen at the center associating with another long stream to the rear of the weld pool. The core of the eddy returns the material to the front surface while the middle paths are responsible for feeding the back region of the weld pool. Some sections of the mentioned eddy are observable near the center

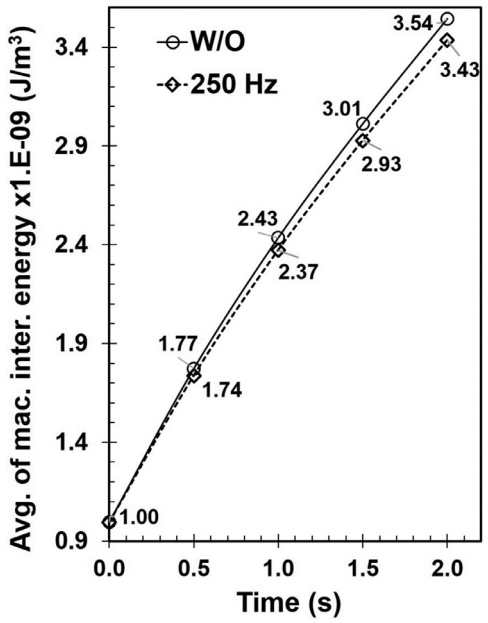

Fig. 14. The average macroscopic internal energy of the occupied cells in the entire domain of W/O vibration and 250 Hz.

and the bottom of the weld pool in Fig. 10(a_1) to (a_3). Investigation of the vibration-assisted sample reveals extremely complicated streams than a W/O vibration case. As illustrated in Fig. 13(c and d), a spiral stream returns the fluid to the free surface from the weld side around the plane of Y=1.5 mm. The behavior of the detected spiral can be seen in more detail in Fig. 10(b_2). In agreement with the discussion on Fig. 11(e), the central plane (Y=0 mm) does not involve material raising in the rear region of the welding. The other important set of streams are found in the droplet path while carrying the high-temperature material to the surface after travelling from the bottom of the weld pool (see black arrow in Fig. 12e). The contour of internal energy is employed to represent an energetic view of the welding process. As illustrated in Fig. 13, the internal energy of the central layer enhances in the presence of the vibration. The average macroscopic internal energy of the occupied cells in the entire domain, including workpiece and the weld pool, reveals a higher value in W/O vibration certainly because of the higher heat input. Fig. 14 shows the result of the change in average internal energy in five time-steps of the simulation. With respect to the higher rate of increment in W/O vibration, applying the vibration would change the distribution of macroscopic internal energy by affecting the dynamic balance of the weld pool.

Thermodynamically, the vibration of a viscous fluid with the free surface increases the internal energy; however, in this study, the enhancement value is found negligible in comparison to the heat input reduction. The investigation primarily divulges the complex interactions between workpiece vibration and weld pool formation in tandem pulsed GMAW. Inclusion of mutual arc interaction in tandem welding and induced arc stability because of dissimilar currents at the trailing and leading electrode [50] in the vibration model will advance the vibration model in future. Besides, the impact of vibration frequency, peak acceleration, or the sulfur concentration on the arc and weld pool interaction merits further investigation.

5. Conclusions

In this study, a novel three-dimensional numerical model of the TP-GMAW process is successfully simulated for the first time to investigate the heat transfer and material flow in the presence of surface tension active elements and the workpiece vibration. The validity of the simulation results is investigated by optical microscopy images obtained for different conditions of welding. The results can be summarized as follows:

(1) The material flow is traced using streamline and temperature color maps. A unique set of 3D streamlines is introduced for visualizing the complicated material flow in TP-GMAW process. It is found during the operation of pulsed welding, the heat flow demonstrated a very stable pattern, although the fluid streams constantly changed in the rear region of the weld pool.
(2) Consideration of the effect of surface tension active elements on the Marangoni force leads to more reliable simulation results. The sulfur content in the filler material improves the penetration depth by reducing the negative gradient of surface tension in Fe–C alloy. The effect of sulfur on the creation of both negative and positive gradient of surface tension during welding is discussed by a novel approach.
(3) The vibration affects the free surface behavior that leads to a change in heat input through a synergic welding machine and thereby plays an important role in the penetration shape change. The internal energy variation due to the physical movement of vibration is not detected based on the simulation results; however, change in the dynamic balance of the weld pool directly affects the distribution of internal energy.

Declaration of Competing Interest

The authors declare that there is no conflict of interest.

CRediT authorship contribution statement

H. Hamed Zargari: Formal analysis, Software, Visualization, Writing - original draft. **K. Ito:** Conceptualization, Project administration, Resources. **M. Kumar:** Investigation. **A. Sharma:** Resources, Writing - review & editing.

Acknowledgments

This research was supported by The Joint Usage/Research Center on Joining and Welding, Osaka University, and also by Project to Create Research and Educational Hubs for Innovative Manufacturing in Asia, Osaka University, funded by Special Budget Project of the Ministry of Education, Culture, Sports, Science and Technology. Acknowledgements are due to Manufacturing Laboratory at IITH for providing facilities for experiments.

References

[1] Y. Hirata, Pulsed arc welding, Weld. Int. 17 (2003) 98–115.
[2] B.Y.B. Yudodibroto, M.J.M. Hermans, G. den Ouden, I.M. Richardson, Observations on droplet and arc behaviour during pulsed GMAW, Weld. World 53 (2009) 171–180.
[3] U.K. Mohanty, Y. Abe, T. Fujimoto, M. Nakatani, A. Kitagawa, M. Tanaka, T. Suga, A. Sharma, Performance evaluation of alternating current square waveform submerged arc welding as a candidate for fabrication of thick welds in 2.25Cr-1Mo heat-resistant steel, J. Press. Vessel Technol. 142 (2020).
[4] K. Wu, N. Ding, T. Yin, M. Zeng, Z. Liang, Effects of single and double pulses on microstructure and mechanical properties of weld joints during high-power double-wire GMAW, J. Manuf. Process. 35 (2018) 728–734.
[5] M.J. Jose, S.S. Kumar, A. Sharma, Vibration assisted welding processes and their influence on quality of welds, Sci. Technol. Weld. Join. 21 (2016) 243–258.
[6] E.G. Ramos, G.C. de Carvalho, S.C. Absi Alfaro, Analysis of weld pool oscillation in GMAW-P by means of shadowgraphy image processing, Weld. Int. 29 (2015) 197–205.
[7] H. Matsui, T. Chiba, K. Yamazaki, Detection and amplification of the molten pool natural oscillation in consumable electrode arc welding, Weld. Int. 28 (2013) 5–12.
[8] H. Matsui, S. Shionoya, Reduction of blowholes by vibration of the molten pool in arc welding of galvanised carbon steel sheet, Weld. Int. 12 (1998) 959–965.

[9] H. Hamed Zargari, K. Ito, T. Miwa, P.K. Parchuri, H. Yamamoto, A. Sharma, Metallurgical characterization of penetration shape change in workpiece vibration-assisted tandem-pulsed gas metal arc welding, Material 13 (2020) 3096.
[10] H.H. Zargari, K. Ito, Y. Mikami, A. Sharma, A unique CEL numerical method on material flow in a molten pool of workpiece vibration assisted welding, Q. J. Jpn. Weld. Soc. (2020) 54–58.
[11] K.C. Tsao, C.S.C.S. Wu, Fluid flow and heat transfer in GMA weld pools determination of the electromagnetic, Weld. J. 03 (1988) 70s.
[12] M. Ushio, C.S. Wu, Mathematical modeling of three-dimensional heat and fluid flow in a moving gas metal arc weld pool, Metall. Mater. Trans. B Process. Metall. Mater. Process. Sci. 28 (1997) 509–516.
[13] N.D. Katopodes, Chapter 12 – Volume of Fluid Method, in: Free-Surface Flow: Computational Methods, Butterworth-Heinemann, 2019, pp. 766–802.
[14] X.L.C.Z. Cao, Z. Yang, Three-dimensional simulation of transient gma weld pool with free surface, Weld. J. (2004) 169–176.
[15] M.H. Cho, Y.C. Lim, D.F. Farson, Simulation of weld pool dynamics in the stationary pulsed gas metal arc welding process and final weld shape, Weld. J. 85 (2006) 271–283.
[16] J. Hu, H. Guo, H.L. Tsai, Weld pool dynamics and the formation of ripples in 3D gas metal arc welding, Int. J. Heat Mass Transf. 51 (2008) 2537–2552.
[17] D.B. Kothe, R.C. Mjolsness, RIPPLE – A new model for incompressible flows with free surfaces, AIAA J. 30 (1992) 2694–2700.
[18] D. Gueyffier, J. Li, A. Nadim, R. Scardovelli, S. Zaleski, Volume-of-fluid interface tracking with smoothed surface stress methods for three-dimensional flows, J. Comput. Phys. 152 (1999) 423–456.
[19] J.E. Pilliod, E.G. Puckett, Second-order accurate volume-of-fluid algorithms for tracking material interfaces, J. Comput. Phys. 199 (2004) 465–502.
[20] M. Barkhudarov, Lagrangian VOF Advection method for FLOW-3D, Flow Sci. Inc. (2004) 1–11 FSI-03-TN6.
[21] J. Cheon, D.V. Kiran, S.J. Na, CFD based visualization of the finger shaped evolution in the gas metal arc welding process, Int. J. Heat Mass Transf. 97 (2016) 1–14.
[22] D. Wu, S. Tashiro, Z. Wu, K. Nomura, X. Hua, M. Tanaka, Analysis of heat transfer and material flow in hybrid KPAW-GMAW process based on the novel three dimensional CFD simulation, Int. J. Heat Mass Transf. 147 (2020) 118921.
[23] K. Park, H. Jeong, S. Baek, D.Y. Kim, M.J. Kang, J. Cho, Turbulent molten pool analysis of tandem GMA automotive steel sheet welding, Int. J. Heat Mass Transf. 129 (2019) 1–6.
[24] Z. Yang, T. Debroy, Modeling macro-and microstructures of gas-metal-arc, Metall. Mater. Trans. B 30 (1999) 483–493.
[25] B.J. Keene, K.C. Mills, J.W. Bryant, E.D. Hondros, Effects of interaction between surface active elements on the surface tension of iron, Can. Metall. Q. 21 (1982) 393–403.
[26] P. Sahoo, T. Debroy, M.J. McNallan, Surface tension of binary metal-surface active solute systems under conditions relevant to welding metallurgy, Metall. Trans. B 19 (1988) 483–491.
[27] K.C. Mills, B.J. Keene, Factors affecting variable weld penetration, Int. Mater. Rev. 35 (1990) 185–216.
[28] Y. Wang, H.L. Tsai, Effects of surface active elements on weld pool fluid flow and weld penetration in gas metal arc welding, Metall. Mater. Trans. B Process Metall. Mater. Process. Sci. 32 (2001) 501–515.
[29] Z. Gan, G. Yu, X. He, S. Li, Surface-active element transport and its effect on liquid metal flow in laser-assisted additive manufacturing, Int. Commun. Heat Mass Transf. 86 (2017) 206–214.
[30] J. Zhao, G. Wang, X. Wang, S. Luo, L. Wang, Y. Rong, Multicomponent multiphase modeling of dissimilar laser cladding process with high-speed steel on medium carbon steel, Int. J. Heat Mass Transf. 148 (2020) 118990.
[31] FLOW-3D user's manual, Inc., Flow Sci. v11.2 (2018).
[32] B. Leffler, S. Malm, Volume changes accompanying solidification of some austenitic stainless steels, Met. Technol. 4 (1977) 81–90.
[33] A. Joseph, D. Harwig, D.F. Farson, R. Richardson, Measurement and calculation of arc power and heat transfer efficiency in pulsed gas metal arc welding, Sci. Technol. Weld. Join. 8 (2003) 400–406.
[34] Y. Wang, H.L. Tsai, Impingement of filler droplets and weld pool dynamics during gas metal arc welding process, Int. J. Heat Mass Transf. 44 (2001) 2067–2080.
[35] D.W. Cho, S.J. Na, M.H. Cho, J.S. Lee, Simulations of weld pool dynamics in V-groove GTA and GMA welding, Weld. World 57 (2013) 223–233.
[36] W. Zhang, C.H. Kim, T. DebRoy, Heat and fluid flow in complex joints during gas metal arc welding – Part I: Numerical model of fillet welding, J. Appl. Phys. 95 (2004) 5210–5219.
[37] D.J. Phares, G.T. Smedley, R.C. Flagan, The wall shear stress produced by the normal impingement of a jet on a flat surface, J. Fluid Mech. 418 (2000) 351–375.
[38] M.R.U. Ahsan, M. Cheepu, R. Ashiri, T.H. Kim, C. Jeong, Y. Do Park, Mechanisms of weld pool flow and slag formation location in cold metal transfer (CMT) gas metal arc welding (GMAW), Weld. World 61 (2017) 1275–1285.
[39] K.C. Tsao, C.S. Wu, Modelling the three-dimensional fluid flow and heat transfer in a moving weld pool, Eng. Comput. 7 (1990) 241–248.
[40] A. Kumar, T. DebRoy, Calculation of three-dimensional electromagnetic force field during arc welding, J. Appl. Phys. 94 (2003) 1267–1277.
[41] T. Ueyama, T. Ohnawa, M. Tanaka, K. Nakata, Occurrence of arc interaction in tandem pulsed gas metal arc welding, Sci. Technol. Weld. Join. 12 (2007) 523–529.
[42] M.S. Min Hyun Cho, Numerical Simulation of Arc Welding Process and Its Application, The Ohio State University, 2006.
[43] C. McIntosh, J. Chapuis, P.F. Mendez, Effect of Ar-CO_2 gas blends on droplet temperature in GMAW, Weld. J. 95 (2016) 273s–279s.
[44] E.J. Soderstrom, K.M. Scott, P.F. Mendez, Calorimetric measurement of droplet temperature in GMAW, Weld. J. 90 (2011).
[45] N.S. TSAI, T.W. EAGAR, Distribution of the heat and current fluxes in gas tungsten arcs, 16 (1985) 841–846.
[46] M.L. Lin, T.W. Eagar, Pressures produced by gas tungsten arcs, Metall. Trans. B 17 (1986) 601–607.
[47] H.P. Ebert, S. Braxmeier, D. Neubert, Intercomparison of thermophysical property measurements on iron and steels, Int. J. Thermophys. 40 (2019) 1–18.
[48] B. Pollard, Effects of minor elements on the welding characteristics of stainless steel., Weld. J. 67 (1988).
[49] Tecplot 360 ex User's manual, Inc., Tecplot. (2019).
[50] M. Kumar, S. Quadir Moinuddin, S.S. Kumar, A. Sharma, Discrete wavelet analysis of mutually interfering co-existing welding signals in twin-wire robotic welding, J. Manuf. Process (2020) doi.org/, doi:10.1016/j.jmapro.2020.04.048.